NANO LETTERS

2008
Vol. 8, No. 5
1296-1302

Acoustic Vibration Modes and Electron–Lattice Coupling in Self-Assembled Silver Nanocolumns

J. Burgin,[†] P. Langot,[†] A. Arbouet,[*,‡] J. Margueritat,[‡,§] J. Gonzalo,[§] C. N. Afonso,[§] F. Vallée,[||] A. Mlayah,[‡] M. D. Rossell,[⊥] and G. Van Tendeloo[⊥]

CPMOH, Université Bordeaux 1, 351 cours de la Libération, 33405 Talence Cedex France, CEMES, CNRS/Université Toulouse, 29 rue Jeanne Marvig, BP 94347, 31055 Toulouse, France, Laser Processing Group, Instituto de Optica, CSIC, Serrano 121, 28006 Madrid, Spain, LASIM, Université Lyon 1, CNRS, 43 bd du 11 Novembre 1918, 69622 Villeurbanne, France, and EMAT, University of Antwerp, Groenenborgerlaan 171, B-2020 Antwerp, Belgium

Received November 30, 2007; Revised Manuscript Received March 5, 2008

ABSTRACT

Using ultrafast spectroscopy, we investigated electron–lattice coupling and acoustic vibrations in self-assembled silver nanocolumns embedded in an amorphous Al_2O_3 matrix. The measured electron–lattice energy exchange time is smaller in the nanocolumns than in bulk silver, with a value very close to that of isolated nanospheres with comparable surface to volume ratio. Two vibration modes were detected and ascribed to the breathing and extensional mode of the nanocolumns, in agreement with numerical simulations.

Downsizing a material to the nanometer scale leads to large modifications of its electronic and vibrational properties. A better understanding of the impact of size, shape, or environment on its electronic and vibrational properties will open the route toward a precise tailoring of these materials to specific applications. For instance, the effect of confinement on the ultrafast electronic processes in metallic nanoparticles has been extensively studied using time-resolved pump–probe spectroscopy.[1–6] The vibrational properties of these systems have first been investigated by spontaneous Raman scattering in which the quadrupolar vibration modes yield the stronger signals.[7–9] In time-resolved experiments, coherent excitation of the acoustic radial modes gives rise to a strong modulation of the optical properties of the nanosystem allowing measurement of both its period and damping time.[10–12] Such measurements have recently been reported in nanosized metallic systems with different shapes and structures.[14–16] With the development of advanced synthesis techniques, new nanomaterials and nano-objects with well-controlled size and shape can now be created. In particular, silver nanocolumns (NCls) embedded in amorphous Al_2O_3 matrix (a-Al_2O_3) have recently been fabricated by self-assembling using alternate pulsed laser deposition.[17] This technique has proven its potential for the production of silver nanocolumns oriented perpendicularly to the substrate with low size and shape dispersion. Earlier reported extinction spectra of these NCls exhibit two distinct optical resonances due to the transverse and longitudinal surface plasmons.[3,18] Raman spectroscopy has given insight into their vibrational dynamics, but these experiments addressed vibration modes involving displacement in the transverse direction, only. No evidence for vibration modes involving displacement along the longitudinal direction was obtained.[18]

In this work, we report on time-resolved pump–probe experiments on silver nanocolumns embedded in amorphous Al_2O_3. We first focus on the electron–lattice energy exchange. The measured characteristic time of this thermalization process is smaller than that in bulk silver.[5] A second set of experiments addressed the vibrational dynamics. Two vibration modes have been detected that did not show up in low-frequency Raman experiments.[18] The period of one of them is proportional to the NCls height, in good agreement with calculations for the extensional mode. In contrast, the period of the second mode is independent of the NCls height, and it has been identified with their breathing mode. The frequencies of all the observed vibrations are consistent with numerical simulations using the acoustic constants of bulk silver, supporting fabrication of a continuous structure. In previous time-resolved experiments on gold nanorods,[13] the

* Corresponding author: arnaud.arbouet@cemes.fr.
[†] CPMOH, Université Bordeaux 1.
[‡] CEMES, CNRS/Université Toulouse.
[§] Laser Processing Group, Instituto de Optica, CSIC.
[||] LASIM, Université Lyon 1.
[⊥] EMAT, University of Antwerp.

10.1021/nl073123r CCC: $40.75
Published on Web 04/01/2008

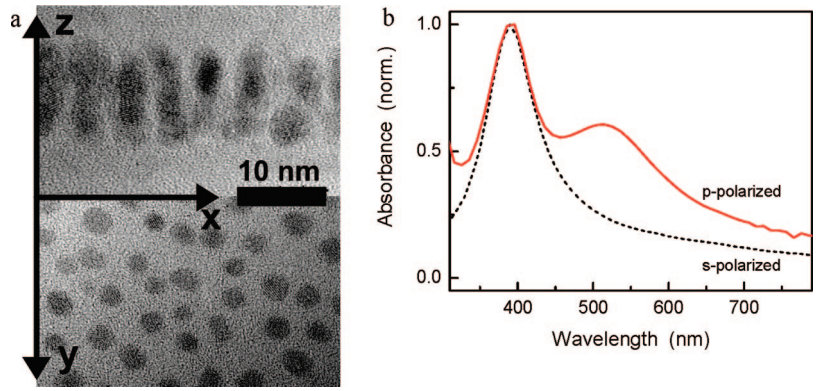

Figure 1. (a) Cross section (z) and plan view (x,y) images of the sample N10a containing self-assembled NCls embedded in a-Al_2O_3 matrix. This sample was produced with 10 cycles. (x,y) is the substrate plane. (b) Corresponding experimental extinction spectra recorded with s- and p-polarized light. The curves have been slightly shifted along the y-direction for more clarity.

extensional mode has been detected probing in the vicinity of the longitudinal plasmon band. Indeed, the displacement associated with this vibration mode leads to larger signals in this spectral region. In our case, the very high sensitivity of the experimental setup allows detecting both vibration modes with probe energy close to the transverse surface plasmon resonance. In addition, the time-resolved data provide information on the damping of these modes.

The samples studied in this work have been produced by alternate pulsed laser deposition in vacuum (10^{-6} mbar) using an ArF excimer laser (pulse duration 20 ns, energy density 1.9 J·cm^{-2}). The beam was sequentially focused on the surface of high-purity Al_2O_3 and Ag rotating targets. First, a layer of amorphous Al_2O_3 was deposited to serve as substrate where a layer of Ag nanoparticles (Nps) nucleated following the Volmer–Weber growth mode of metal on an oxide surface.[18,19] Then the spaces among the Nps were filled with an additional layer of a-Al_2O_3. The so-obtained layer is used as a template in which the preferential sites for the nucleation are located on top of the NPs. The Ag atoms arriving consecutively nucleate preferentially on these sites, leading to the production of self-aligned NCls.[17] Each sample consists in n cycles of ablation metal-matrix, thus leading to one layer of NCls with an increasing height as n increases from 5 to 20. The films were simultaneously produced on a silicon substrate for transmission electron microscopy (TEM) cross-sectional studies and low-frequency Raman spectroscopy, and on a glass substrate for absorption measurements and time-resolved experiments, and on carbon-coated mica for TEM plan view analysis.

The morphology and structure of the films have been studied by transmission electron microscopy (TEM) with a JEOL 4000EX microscope operating at 400 kV with a point to point resolution of 0.17 nm. The cross-sectional specimens have been prepared by focused ion beam (FIB) with internal lift out using a FEI Nova 200 NanoLab dual beam SEM/FIB system. This study has confirmed that the specimens consist in NCls with characteristic dimensions summarized in Table 1. In the case of $n = 10$, NCls with different aspect ratios were produced by changing the ablation time of Ag and Al_2O_3. Figure 1a shows a top view and a cross-section

Table 1. Number of Cycles n, Average In-Plane Diameter $\langle D \rangle$, and Height $\langle H \rangle$

sample name	no. of cycles (n)	$\langle D \rangle$ (fwhm) (nm)	$\langle H \rangle$ (fwhm) (nm)
N5	5	2.4 (0.2)	6.5 (0.2)
N10a	10	2.4 (0.2)	8.6 (0.2)
N10b	10	2.1 (0.2)	12.4 (0.3)
N20	20	2.4 (0.2)	13 (1)

In parentheses is given the full width at half-maximum (fwhm) of the respective statistical distribution.

view corresponding to the sample N10a; the NCls appear as dark areas. All NCls are polycrystalline and oriented perpendicularly to the substrate ((x, y) plane). We can also observe in the cross-section view that the NCls are not always perfectly continuous, instead their shape looks like a "nano-peanut" rather than a prolate or cylindrical NCl.

Figure 1b shows the extinction spectra of sample N10a obtained with s- or p-polarized incident light. As expected, a single band around 390 nm is observed with s-polarized light. It is due to the transverse SPR because of the in plane circular symmetry of the NCls. In the case of p-polarized light the spectrum shows two bands, at 390 nm (same as for s-polarized), and 540 nm, due to the transverse and longitudinal SPR,respectively.[3] The observed longitudinal-transverse surface plasmon splitting is much smaller than the one calculated for isolated NCls. This is most likely due to the small separation between adjacent NCls and their side-by-side orientational assembling[3,18,20] which allows strong interaction between the localized surface plasmons.

Time-resolved experiments were performed in a two-color configuration with the incident pump and probe beams quasi-normal to the sample surface. The experimental setup is based on a homemade 15 fs Ti-sapphire oscillator working at 860 nm with a 80 MHz repetition rate. The pulse train is split into two beams, one of them being frequency-doubled in a 100 μm thick BBO crystal, to create the pump and probe pulses at two different wavelengths. The pump-induced change of the probe transmission $\Delta T/T$ is detected using a standard pump–probe setup with mechanical chopping of the pump beam at 1.5 kHz and lock-in and differential detection of the transmitted probe energy. The high stability and repetition rate of our setup enable us to achieve high

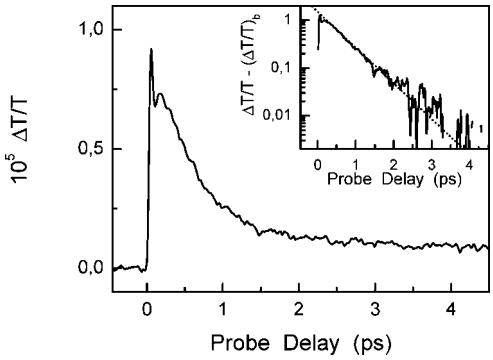

Figure 2. Temporal evolution of the transmission change $\Delta T/T$ measured in sample N5 ($D = 2.4$ nm and $H = 6.5$ nm). The pump and probe wavelengths are 430 and 860 nm, respectively. The inset shows the same data after subtraction of the long delay background fitted by an exponential decay with a coupling time $\tau_{e\text{-}ph} = 580$ fs (dotted line), on a logarithmic scale.

sensitivity measurements with a noise level in the 10^{-7} range, after averaging over 100 scans, i.e., for about 1 h for the pump–probe time-delay window used here.

First, we report on measurements of the electron–lattice energy exchange in the silver nanocolumns. In the pump–probe experiments, the conduction electrons of the metallic nanocolumns are first driven out of equilibrium by intraband absorption of the pump pulse at 430 nm (the pump photon energy is smaller than the interband transition threshold of 3.9 eV in silver). Following optical excitation, electrons redistribute their excess energy among themselves via electron–electron scattering yielding a Fermi−Dirac distribution at higher temperature in a few hundred femtoseconds (350 fs in bulk silver).[21,22] Thermalization of the whole nanoparticle (electron gas and lattice) is achieved by electron–lattice energy exchange on a slightly longer picosecond time scale.[1–6,21–23] The excess energy of the nanoparticle is subsequently damped to the matrix on a few tens of picoseconds. The energy losses from the electron gas to the lattice of the silver NCls were probed in the near-infrared region. In this configuration the measured sample transmission change $\Delta T/T$ is not influenced by the details of the electronic distribution and is almost proportional to the energy excess of the electron gas.[21–23] Figure 2 shows the $\Delta T/T$ signal measured on sample N5. After a sharp rise in the first hundreds of femtoseconds following energy injection, $\Delta T/T$ decreases due to energy losses from the electron gas to the lattice. Assuming that both the electron gas and the lattice are thermalized, these energy exchanges can be described using the two-temperature model.[24,25] In the low perturbation regime (electronic temperature rise smaller than 200 K), this model predicts a monoexponential decay of the electronic excess energy with a characteristic time $\tau_{e\text{-}ph}$. The latter can thus be extracted by fitting a monoexponential decay to the experimental data (Figure 2).

We have obtained a characteristic time $\tau_{e\text{-}ph}$ very close to 580 fs in all the studied samples. This value is much smaller than the one, 870 fs, determined for bulk silver indicating a faster electron–lattice thermalization in the NCls. Previous systematic investigations of the size effects on the electron internal thermalization and electron–lattice thermalization in spherical metal nanoparticles have pointed out an acceleration of these electronic processes with decreasing size. Though a full theoretical model has still to be developed, this has been attributed to enhancement of the electron-ion coupling close to the nanoparticle surface due to reduction of the screening of the Coulombic interactions.[5,21] The role of this effect increases with size reduction, i.e., as the impact of surface effects increases as compared to volume ones.[5] As a first approximation the electron–lattice energy exchange rate can thus be written as the sum of a volume and a surface contribution. The latter is responsible for increase of the electron–lattice coupling with nanoparticle size reduction, with an amplitude proportional to the nanoparticle surface over volume ratio. This simple argument is in very good agreement with our results in silver NCls. Actually, the characteristic time $\tau_{e\text{-}ph}$ measured here corresponds to that in silver nanospheres with a diameter between 3 and 4 nm.[5] Very interestingly, the surface to volume ratio of our NCls is the same as that of nanospheres with diameter between 3 and 3.3 nm. As in nanospheres, we thus ascribe reduction of the electron–lattice energy exchanges in NCls to surface effects.

We performed a second set of experiments addressing specifically the vibrational properties of the NCls. Following excitation by an ultrashort pump pulse, thermal expansion of the lattice is induced either directly (electron pressure) or indirectly (lattice heating). This excitation process, shorter than the period of the low-frequency acoustic vibration modes, will launch impulsively acoustic vibrations associated to a volume change of the NCls.[11,12] In the particular case of pump–probe experiments in nanorods only two types of vibration eigenmodes are excited: the radial and the extensional modes.[26] The fundamental radial mode, the so-called breathing mode, involves a periodic radial expansion-contraction displacement in the transverse direction. The fundamental extensional mode involves expansion in the longitudinal direction with a smaller contraction in the transverse one. For a perfect free nanocolumn (cylinder with flat end surfaces in vacuum) of large aspect ratio, the period of the radial breathing mode of order n is given by[26]

$$T_{\mathrm{br,cyl}}^{\mathrm{free}\ (n)} = \frac{\pi D}{\phi_n c_{\mathrm{L}}} \tag{1}$$

where D is its diameter and c_{L} is the longitudinal speed of sound. φ_n is a solution of $\phi_n J_0(\phi_n) = (1 - 2\nu) J_1(\phi_n)/(1 - \nu)$, ν being Poisson's ratio and J_0 and J_1 are Bessel functions of the first kind of orders 0 and 1, respectively.

The period of the extensional mode of order n is

$$T_{\mathrm{br,cyl}}^{\mathrm{free}\ (n)} = \frac{2H}{(2n+1)\sqrt{E/\rho}} \tag{2}$$

where H is the height of the nanocolumn, E is its Young's modulus, and ρ is its density.[26] The excited acoustic vibrations modulate both the volume (leading, as in nanosphere, to modulation of the metal dielectric function via change of the electronic bands and electron density) and the aspect ratio of the nanocolumns. Both effects lead to frequency modulation of both the transverse and longitudinal

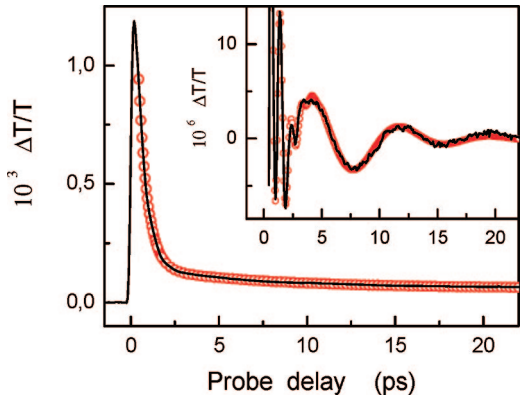

Figure 3. (Full line) Time dependence of the transmission change $\Delta T/T$ measured in sample N10b. (Open circles) Fit by the sum of two exponentials associated with the electron–lattice thermalization and the nanocolumn-to-matrix energy damping contributions. Inset: Oscillating component of the signal obtained as the difference between the two previously mentioned curves (full line) and numerical fit of the oscillating part with two damped cosine functions (dashed line). The pump and probe photon wavelengths are 860 and 430 nm, respectively.

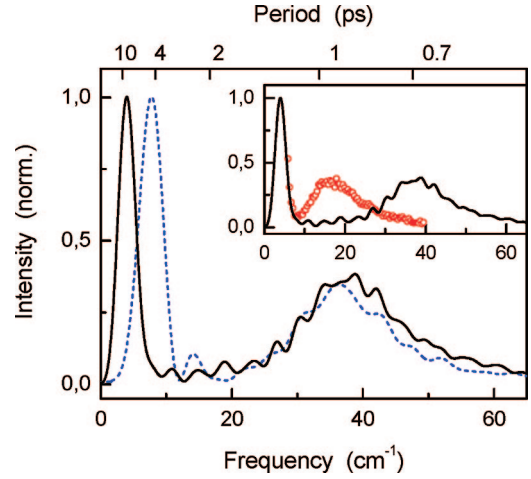

Figure 4. Fast Fourier transform of the oscillating part of $\Delta T/T$ measured in samples N5 (blue dashed line) and N10b (full line) and low-frequency Raman spectrum measured in sample N10b (red circles).

plasmon resonances which shows up as oscillations in the relative transmission change.[11,12]

To improve the sensitivity of the measurements to modulation of the surface plasmon resonance wavelength, the sample is here excited by the near-infrared pulses and probed at 430 nm.[11,12] As shown in Figure 3, the relative transmission change displays very small oscillations which partially overlap with its short and long delay decays reflecting electron–lattice thermalization and damping of the nanocolumn energy to the matrix, respectively. The nonoscillating part of the signal can be reproduced as a sum of two exponentially decaying contributions with times 550 fs and 7.5 ps, reflecting these mechanisms. As expected, the former is in excellent agreement with the electron–lattice coupling time measured in the first set of experiments (Figure 2). The difference between the experimental data and the fit reveals a residual oscillating contribution (Figure 3, inset). Two vibration modes are clearly visible: one with a period of about 0.9 ps in the first 3 ps and a long period one in the following 20 ps.

Fast Fourier transform (FFT) analysis of the time-resolved data clearly displays two bands (Figure 4). The first one around 38 cm^{-1} ($T = 0.88$ ps) corresponds to the fastest oscillations detected in the first 4 ps. Its frequency does not depend on the height of the NCls. The second one corresponds to slower oscillations and strongly shifts to lower frequency as the height of the NCls increases. In Figure 4 is also plotted the low-frequency Raman spectrum of one sample.[18] Only one vibration band is detected in the Raman spectra. Its frequency is independent of the NCls height[8] and is very different from the frequencies measured using time-resolved spectroscopy. This illustrates the very different nature of light−matter interaction in Raman and time-resolved experiments:[27] the detected acoustic vibration modes and their relative intensities are different. Time-domain experiments performed on spherical particles with diameter $D = 2.7$ nm dispersed in a-Al_2O_3 matrix yielded only one mode at 48 cm^{-1} (i.e., a period of 0.70 ± 0.05 ps). It is in good agreement with the prediction of Lamb theory for the period of the fundamental breathing mode of silver nanospheres with diameter $D = 2.7$ nm in a-Al_2O_3 matrix ($T^{\text{alum}}_{\text{br,sphere}} = 0.68$ ps). The absence of a second mode confirms that the low-frequency mode is specific to the elongated objects.

We performed systematic measurements for different NCls heights. In all cases, the periods yielded by the FFT analysis have been confirmed by direct fitting of the time-resolved data using the linear prediction singular value decomposition (LPSVD) technique. More importantly, this analysis gives access to the damping time and phase of the oscillations of each of the two observed modes. They will be discussed in the last part of the paper. Figure 5 shows the period of the high (a) and low (b) frequency modes as a function of the NCls height H. The period of the high-frequency mode is independent of H and is very close to the period $T^{\text{free}}_{\text{br,cyl}} = 0.93$ ps of the fundamental breathing mode of a free silver nanorod with diameter $D = 2.4$ nm given by eq 1 (Figure 5b). In addition, the measured periods are clearly larger than that of the breathing mode of a spherical particle with same diameter confirming a shift from spherical to elongated object during the deposition process. In contrast, the period of the lowest frequency mode exhibits a linear dependence on the NCls height (Figure 5b). The measured periods are consistent with those calculated for the extensional mode of a free nanorod (eq 2). Therefore, we ascribed the low-frequency vibration mode to the extensional mode of the NCls and the higher frequency mode to their breathing mode.

However, the free nanorod model underestimates the oscillation periods of the extensional mode. A possible explanation might be the influence of the matrix. However, inclusion of the stress-induced matrix effect on the NCls is expected to reduce the oscillation periods leading to a larger discrepancy between the calculated and the measured values. This effect can be illustrated in the case of nanospheres for which a theoretical model has been developed: the period of the fundamental breathing mode of silver nanospheres with diameter $D = 2.7$ nm predicted by Lamb theory is $T^{\text{free}}_{\text{br,sphere}}$

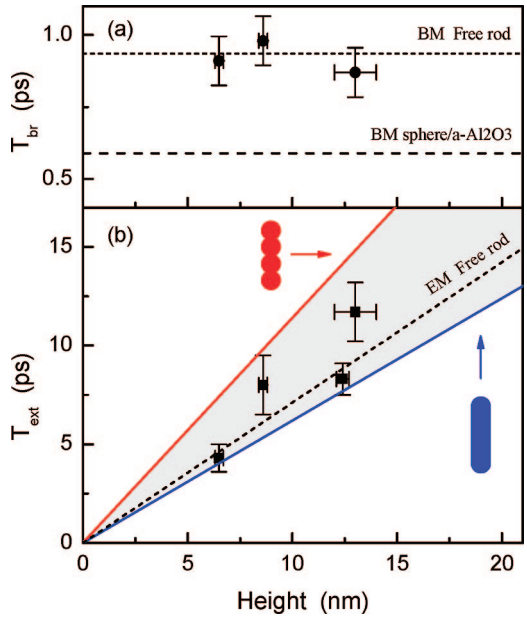

Figure 5. (a) Measured periods of the high-frequency vibration mode of silver NCls in a-Al_2O_3 with diameter 2.4 nm and length from 6.5 to 13 nm (circles). Computed period of the fundamental breathing mode (BM) of a free silver nanorod with diameter 2.4 nm (dotted line) and computed period of the fundamental breathing mode of a silver spherical nanoparticle with diameter 2.4 nm in a-Al_2O_3 (dashed line). (b) Measured periods of the low-frequency vibration mode of silver NCls (squares) and computed period of the extensional mode (EM) of a free silver nanorod using eq 2 (dotted line). The colored area is delimited by two straight lines representing the computed period with finite element analysis considering the two types of structures sketched in the graph and described in the text.

$= 0.82$ ps for a free particle and $T_{br,sphere}^{alum} = 0.68$ ps for a particle embedded in a-Al_2O_3.

Shape effects, i.e., deviations of the investigated NCls from perfect nanorods, is probably at the origin of this discrepancy. To address this point, we calculated the period of the extensional mode of structures mimicking the geometries observed by electron microscopy using finite element analysis (COMSOL 3.2). A nanocolumn has been constructed by stacking of spherical particles with diameter $D = 2.4$ nm partially overlapping, the distance between the centers of adjacent spheres being d. We assumed a continuous, homogeneous and isotropic medium and used the elastic parameters of bulk silver (Young's modulus $E = 83$ GPa, Poisson's ratio $\upsilon = 0.36$, and density $\rho = 10\ 490$ kg/m^3). Free boundary conditions (Neumann boundary conditions) were applied. Figure 5 shows the NCls height dependence of the computed periods for two limiting situations: (i) a cylinder with two half-spheres at the edges obtained for very small d; (ii) a nanocolumn with periodic shrinks obtained with $d = 0.9$ D. The calculated periods are always proportional to the height of the nano-object but with a slope about 80% larger for shape i as compared to shape ii, stressing the very strong impact of the shape on the acoustic mode properties. In our systems, imperfections in shape may thus counterbalance the effect of the matrix and reduce the discrepancy between the measured periods and the calculated ones for a free rod. In our case, both effects make difficult observation of a possible size and shape effect on the metal acoustic properties, as suggested by experiments in colloidal solution of gold nanorods.[28]

In all samples, the extensional mode oscillations show a quasi-cosine-like behavior. This is consistent with the phase measured in similar conditions in large spherical nanoparticles (typically $D \geq 20$ nm), i.e., associated to a long period breathing mode.[12] As in the latter this suggests that excitation is dominated by the lattice-mediated displacive mechanism due to fast lattice heating.[12–14] In contrast, the phase of the NCls breathing mode is shifted by about $\pi/4$ in all the investigated samples suggesting that both the indirect (lattice heating) and direct (electron pressure) mechanisms[12] contribute to its impulsive launching. This increased role of the electron pressure mechanism is fully consistent with the small period of the breathing mode (0.93 ps), making this transient mechanism more probable and concomitantly reducing the role of the displacive excitation. More quantitatively, assuming that, as in nanospheres, the vibration modes can be modeled by damped harmonic oscillators and using the Grüneisen parameter ratio deduced from nanosphere data,[12] the electron pressure mechanism is estimated to contribute 10 times less to the excitation of the extensional mode than the indirect mechanism, while the contributions become comparable for the breathing mode. However, we emphasize here that in the case of nanocolumns, the simple oscillator model can only yield a crude description of the mode launching due to the complex displacement field associated with their vibration (as compared to spheres).[26] A more precise description of the experimentally measured phases thus requires a model properly taking into account this displacement.

One of the main interests of time-resolved experiments lies in their ability to provide information on the vibration mode damping. Damping of the oscillations measured in the time domain are known to be due to both acoustic energy transfer to the particle environment (homogeneous damping) and to dephasing of the contribution of the different nanoparticles that oscillate with slightly different period imposed by their shape and size.[11] When the latter inhomogeneous contribution, that reflect samples polydispersity,[11,29] is small enough or when dispersity is precisely known, information on the nanoparticle−environment coupling can be obtained.[11] We measured a damping time for the breathing mode oscillations close to 1 ps in all the investigated samples. This is longer for the extensional mode, with experimental values of 4, 6, and 11 ps for samples N5, N10b, and N20, respectively.

To analyze the origin of this damping, influence of polydispersity has been estimated assuming that the breathing and extensional mode periods are proportional to the NCls diameter and height, respectively, and using the measured size distribution. Neglecting the size dependence of the damping time and phase of the oscillations for our narrow

size distribution samples, the measured signal can be written as the sum of the contribution of each nanocolumn:[11]

$$S_{\mathrm{br}}(t) = \mathrm{e}^{-t/\tau_{\mathrm{h}}^{\mathrm{br}}} \sum\nolimits_{D} P_D(t) \cos\left(\frac{2\pi}{T_{\mathrm{br}}(D)} t - \phi_{\mathrm{br}}\right) \quad (3)$$

$$S_{\mathrm{ext}}(t) = \mathrm{e}^{-t/\tau_{\mathrm{h}}^{\mathrm{ext}}} \sum\nolimits_{H} P_H(t) \cos\left(\frac{2\pi}{T_{\mathrm{ext}}(H)} t - \phi_{\mathrm{ext}}\right) \quad (4)$$

where $T_{\mathrm{br}}(D)$ and $T_{\mathrm{ext}}(H)$ are the period of the breathing and extensional mode of nanocolumn with diameter D and heignt H, respectively, and $P_D(D)$ and $P_H(H)$ their relative number. $\tau_{\mathrm{h}}^{\mathrm{br}}$ ($\tau_{\mathrm{h}}^{\mathrm{ext}}$) is the homogeneous damping time of the breathing (extensional) mode and φ_{br} (φ_{ext}) its phase. With this approach, inhomogeneous damping times, $\tau_{\mathrm{in}}^{\mathrm{br}}$ and $\tau_{\mathrm{in}}^{\mathrm{ext}}$, are estimated as the time for 1/e decay of the signal neglecting homogeneous damping (i.e, considering only the summation over the individual contributions in eqs 3) and 4). For small inhomogeneous contribution, the homogeneous damping times, $\tau_{\mathrm{h}}^{\mathrm{br}}$ and $\tau_{\mathrm{h}}^{\mathrm{ext}}$, can thus be estimated using: $1/\tau = 1/\tau_{\mathrm{inh}} + 1/\tau_{\mathrm{h}}$. The inhomogeneous damping time is found to be much smaller than the oscillation decay time $\tau^{\mathrm{br}} \approx 1$ ps for the breathing mode, $\tau_{\mathrm{inh}}^{\mathrm{br}} \approx 5.5$ ps, yielding $\tau_{\mathrm{h}}^{\mathrm{br}} \approx 1.2$ ps (a similar result was obtained using direct data fitting with eqs 3 and 4). Its contribution is even smaller in the case of the extensional mode, leading to $\tau_{\mathrm{h}}^{\mathrm{ext}} \approx \tau^{\mathrm{ext}}$ in all investigated samples. Similar conclusions were drawn using an analytic approach assuming a Gaussian size distribution (for which expressions 3 and 4 can be analytically calculated).[29] For both modes, size effect only weakly contributes to the measured oscillation damping. The latter thus provides an estimate of their homogeneous relaxation, keeping in mind that shape effects, included in the inhomogeneous damping estimation, could also play a role but are very difficult to estimate.

The variations of the homogeneous damping times with the diameter and height of the nanocolumns can be understood using a simple qualitative scaling argument: for a given vibration mode, the time necessary to evacuate the energy excess from the NCl to the matrix (homogeneous damping time) can be estimated as the ratio between the energy stored in the particle (proportional to its volume) and the surface through which it flows out of it.[11,12] Homogeneous damping reflects acoustic wave excitation in the matrix due to the vibration of the particle surface. Conversely to sphere, this is not isotropic for columns, the breathing and extensional mode involving mainly displacement perpendicular and along the column axis, respectively. As a first approximation, damping thus mainly involves the lateral and end surface, respectively. Their homogeneous damping time $\tau_{\mathrm{h}}^{\mathrm{br}}$ and $\tau_{\mathrm{h}}^{\mathrm{ex}}$ should then be proportional to $D/4$ and $H/2$, respectively. In particular, $\tau_{\mathrm{h}}^{\mathrm{br}}$ is expected to be independent of the NCl height in agreement with our experimental results yielding $\tau_{\mathrm{h}}^{\mathrm{br}} \approx 1.2$ ps in all the investigated samples. In contrast $\tau_{\mathrm{h}}^{\mathrm{ex}}$ is predicted to increase with the NCl height as observed experimentally. Furthermore, $\tau_{\mathrm{h}}^{\mathrm{ex}}/\tau_{\mathrm{h}}^{\mathrm{br}}$ is expected to be proportional to $2H/D$ consistent with the observed variation with $2H/D \approx 5.4$ and 10.8 and $\tau_{\mathrm{h}}^{\mathrm{ex}}/\tau_{\mathrm{h}}^{\mathrm{br}} \approx 3.3$ and 9, for the smallest and largest height samples (N5 and N20), respectively. Though the experimental damping features are qualitatively explained, a quantitative model of the damping of acoustic modes of nonspherical nanoparticles has to be developed. More precise measurements of the extensional mode damping have also to be performed, for instance, probing closer to the NCls longitudinal plasmon resonance.

In conclusion, the electron–lattice coupling and acoustic vibrations of self-assembled silver nanocolumns embedded in amorphous Al_2O_3 were studied by time-resolved femtosecond spectroscopy. The characteristic time for energy losses from the electron gas to the lattice is very similar to the one obtained in isolated spherical silver nanoparticles having similar surface to volume ratio. On a longer time scale, the relative transmission change when probing close to the transverse plasmon resonance band is modulated by two acoustic vibration modes excited by the laser-induced heating. The low-frequency mode has a period proportional to the height of the nanocolumns. The measured periods are in very good agreement with the calculations for the extensional mode of a nanorod. The high-frequency mode does not depend on the height of the NCl. It has been identified as the breathing mode involving displacement in the transverse direction. The frequencies of all observed vibration modes are consistent with the theoretical models using the acoustic constants of bulk silver supporting the fabrication of a continuous structure. Preliminary results suggest that the damping of these modes is predominantly homogeneous and is much larger for the breathing than extensional mode, in agreement with a simple scaling argument. These first measurements open up the possibility to study shape effect on the acoustic energy transfer at a nanoscale.

Acknowledgment. This work was partially supported by MAT2005-06508-C02-01, MEC (SPAIN), by EU network HPRN-CT-2002-00328, and by CNano GSO program. J.M. acknowledges an I3P fellowship from the CSIC and the European Social Fund.

References

(1) Ahmadi, T. S.; Logunov, S. L.; El Sayed, M. A *J. Phys. Chem.* **1996**, *100* (20), 8053–8056.
(2) Hodak, J. H.; Martini, I.; Hartland, G. V *J. Phys. Chem. B* **1998**, *102* (36), 6958–6967.
(3) Link, S.; El-Sayed, M. A *J. Phys. Chem. B* **1999**, *103* (40), 8410–8426.
(4) Voisin, C.; Del Fatti, N.; Christofilos, D.; Vallée, F *J. Phys. Chem. B* **2001**, *105* (12), 2264–2280.
(5) Arbouet, A.; Voisin, C.; Christofilos, D.; Langot, P.; Fatti, N. D.; Vallée, F.; Lermé, J.; Celep, G.; Cottancin, E.; Gaudry, M.; Pellarin, M.; Broyer, M.; Maillard, M.; Pileni, M. P.; Treguer, M *Phys. Rev. Lett.* **2003**, *90* (17), 177401.
(6) Muskens, O. L.; Del Fatti, N.; Vallée, F *Nano Lett.* **2006**, *6*, 552–556.
(7) Fujii, M.; Nagareda, T.; Hayashi, S.; Yamamoto, K *Phys. Rev. B* **1991**, *44* (12), 6243–6248.
(8) Palpant, B.; Portales, H.; Saviot, L.; Lermé, J.; Prével, B.; Pellarin, M.; Duval, E.; Perez, A.; Broyer, M *Phys. Rev. B* **1999**, *60* (24), 17107–17111.
(9) Portales, H.; Saviot, L.; Duval, E.; Fujii, M.; Hayashi, S.; Del Fatti, N.; Vallée, F *J. Chem. Phys.* **2001**, *115* (8), 3444–3447.
(10) Nisoli, M.; De Silvestri, S.; Cavalleri, A.; Malvezzi, A. M.; Stella, A.; Lanzani, G.; Cheyssac, P.; Kofman, R.; *Phys. Rev. B* **1997**, *55*, R13424.
(11) Del Fatti, N.; Voisin, C.; Chevy, F.; Vallée, F; Flytzanis, C. *J. Chem. Phys.* **1999**, *110*, 11484.
(12) Voisin, C.; Del Fatti, N.; Christofilos, D.; Vallée, F *Appl. Surf. Sci.* **2000**, *164*, 131–139.

(13) Hartland, G. V.; Hu, M.; Wilson, O.; Mulvaney, P.; Sader, J. E *J. Phys. Chem. B* **2002**, *106* (4), 743–747.
(14) Bonacina, L.; Callegari, A.; Bonati, C.; van Mourik, F.; Chergui, M *Nano Lett.* **2006**, *6* (1), 7–10.
(15) Huang, W. Y.; Qian, W.; El-Sayed, M. A *Nano Lett.* **2004**, *4* (9), 1741–1747.
(16) Hodak, J. H.; Henglein, A.; Hartland, G. V *J. Phys. Chem. B* **2000**, *104* (21), 5053–5055.
(17) Margueritat, J.; Gonzalo, J.; Afonso, C. N.; Ortiz, M. I.; Ballesteros, C *Appl. Phys. Lett.* **2006**, *88* (9), 093107.
(18) Margueritat, J.; Gonzalo, J.; Afonso, C. N.; Mlayah, A.; Murray, D. B.; Saviot, L *Nano Lett.* **2006**, *6* (9), 2037–2042.
(19) Barnes, J. P.; Petford-Long, A. K.; Doole, R. C.; Serna, R.; Gonzalo, J.; Suarez-Garcia, A.; Afonso, C. N.; Hole, D *Nanotechnology* **2002**, *13* (4), 465–470.
(20) Jain, P. K.; Eustis, S.; El-Sayed, M. A *J. Phys. Chem. B* **2006**, *110* (37), 18243–18253.
(21) Voisin, C.; Christofilos, D.; Del Fatti, N.; Vallée, F.; Prével, B.; Cottancin, E.; Lermé, J.; Pellarin, M.; Broyer, M.; *Phys. Rev. Lett.* **2000**, *85* (10), 2200–2203.
(22) Del Fatti, N.; Voisin, C.; Achermann, M.; Tzortzakis, S.; Christofilos, D.; Vallée, F.; *Phys. Rev. B* **2000**, *61*, 16956.
(23) Groeneveld, R. H. M.; Sprik, R.; Lagendijk, A *Phys. Rev. B* **1995**, *51* (17), 11433–11445.
(24) Kaganov, M. I.; Lifshitz, I. M.; Tanatarov, L. V. *Eksp. Teor. Fiz.* **1956**, *31*, 232. *Sov. Phys. JETP*, **1957**, *4*, 173.
(25) Allen, P. B. *Phys. Rev. Lett.* **1987**, *59* (13), 1460–1463.
(26) Hu, M.; Wang, X.; Hartland, G. V.; Mulvaney, P.; Juste, J. P.; Sader, J. E *J. Am. Chem. Soc.* **2003**, *125* (48), 14925–14933.
(27) Bachelier, G.; Mlayah, A *Phys. Rev. B* **2004**, *69* (20), 205408–7.
(28) Hartland, G. V. *Phys. Chem. Chem. Phys.* , *6* (23), 5263–5274.
(29) Hartland, G. V. *J. Chem. Phys.* **2002**, *116*, 8048.

NL073123R